Control of a 5DOF Magnetically Levitated Positioning Stage

Cameron Fulford, *Member, IEEE,* Manfredi Maggiore, *Member, IEEE,* and Jacob Apkarian, *Member, IEEE*

Abstract

A high-precision, magnetically levitated, five degree-of-freedom (5DOF) positioning stage is presented. Four independently controlled iron-cored permanent magnet linear synchronous motors are used to translate the stage and rotate it about the two horizontal axes. Six optical encoders with 10 μm resolution, mounted on linear guides, are used to measure displacements and rotations. A detailed mathematical model is developed and nonlinear tracking controllers are designed for the 5DOF system using feedback linearization, output regulation, and antiwindup compensation for step and sinusoidal references.

Index Terms

internal model regulation, magnetic levitation, nonlinear control, PMLSM, positioning stage.

I. Introduction

In recent years, there has been an increased interest in the development of magnetically levitated (maglev) contactless positioning systems with many degrees-of-freedom (DOF) as an alternative to mechanically-driven high-precision positioning systems. Traditional industrial positioning systems are composed of multiple mechanically-driven stages, some of which actuate large, low-resolution movements, while others deliver small, high-resolution motion. Such systems have well-known drawbacks. Friction, stiction, backlash, and hysteresis limit the positioning accuracy. Further, mechanical wear introduces impurities in the form of dust particles into the manufacturing environment. Lastly, mechanical coupling transmits to the microstepper vibrations from the surrounding environment. For those fabrication tasks requiring sub-micrometer accuracy (e.g., photolithography), such vibrations are unacceptable because they significantly affect the performance of the process, so vibration tables are required.

Maglev positioning stages have the potential to eliminate the three problems mentioned above. Being contactless, their positioning accuracy is only limited by the sensor resolution and the control design. They are not subject to mechanical wear and therefore they do not introduce dust particles in the fabrication process. Finally, they are not mechanically coupled to the surrounding environment and are capable, if appropriately controlled, to reject vibrations.

A landmark contribution to the development of high-precision magnetic levitation actuators was given by Kim and Trumper in [1], see also [2]. They developed a 6DOF positioning system using air-cored permanent magnet linear synchronous motors (PMLSMs) with a horizontal displacement range of 50×50 mm^2, a vertical displacement range of 400 μm, and rotations in the mrad range. The position noise was of the order of 5 nm horizontal and 70 nm vertical. The objective of stabilizing set-points in three-space was achieved by means of linearization about equilibria and lead-lag compensators. Since then, other significant contributions were made to the development of high-precision contactless positioning systems. Kim and co-workers [3], [4], [5] developed a compact and lightweight device which employs six Lorentz-type linear air-cored actuators to control 6DOF with a displacement range of $300 \times 300 \times 300$ μm^3, a rotation range of $3.5 \times 3.5 \times 3.5$ mrad^3, and a position noise of about 5 nm. The control specification was set-point stabilization and tracking, and the control design approach is based on feedback linearization and lead-lag compensation. The tracking signals used in the experiments were designed to trace a circle on the horizontal plane and a conical helix in three-space. Menq and co-workers [6], [7], [8], [9] developed three generations of 6DOF devices. The latest prototype, presented in [9], employs three Lorentz-type two-axis linear actuators to achieve a displacement range of $2 \times 2 \times 2$ mm^3, a rotation range of $70 \times 70 \times 70$ mrad^3, and a position noise of about 4nm horizontal and 20 nm vertical. Feedback linearization and loop shaping were used for set-point stabilization and tracking of steps and sinusoids.

Research on maglev systems at the University of Toronto, in collaboration with Quanser, focuses on using combinations of iron-cored PMLSMs to control multiple DOFs. While air-cored PMLSMs in [1] and [2] allow one to levitate the platen above the stators, iron-cored PMLSMs can be used to levitate the platen below the stators. While in air-cored PMLSMs the levitation force is entirely generated by the interaction between the magnetic field of the stator windings and that of the permanent magnets on the mover, in iron-cored PMLSMs most of the levitation force is generated by the attraction between the permanent magnets on the stators, mounted on the platen, and the iron backing of the motors. For this reason, iron-cored

PMLSMs need less current for levitation. In [10], a detailed mathematical model of the forces produced by an iron-cored PMLSM and a nonlinear control design to regulate air-gap and displacement are presented. In [11], these theoretical results are validated on a 2DOF system employing one iron-cored PMLSM. In [11], a 3DOF system employing four PMLSMs to control displacements is also briefly presented. In both setups, linear guides are used to constrain the motion to be purely translational.

Statement of contributions. This paper advances the research presented in [10] and [11] by demonstrating that four independently controlled iron-cored PMLSMs can be used to actuate a platen with 5DOFs: three displacements, and pitch and roll angles. The device presented in this paper is an evolution of the 3DOF device briefly described in [11]. Its range of operation, 100×100 mm^2 horizontal, 13 mm vertical, and rotation range of 6×28 mrad^2, is very large as compared to that of other positioning devices reviewed above. In particular, the use of iron-cored PMLSMs is the key feature that makes it possible to obtain a large vertical displacement. The accuracy of our device is 10 μm for displacements and 20 μrad for rotations. Our device is *not* contactless because it employs linear guides to sense the configuration of the platen, but it is a proof-of-concept giving confidence that our approach can be used to build a next-generation, contactless positioning system based on iron-cored PMLSMs.

We present a detailed mathematical model and introduce a nonlinear control strategy making the displacements and rotations of the platen track step and sinusoidal reference signals. Our control strategy can be summarized as follows. The mathematical model of the system is viewed as a nominal system affected by a perturbation term, which is shown to be negligible. The nominal system is then feedback linearized; a linear output regulator is designed for the feedback-linearized plant, and antiwindup compensation is used to limit the magnitude of the control inputs to within the saturation limits of the amplifiers driving the PMLSMs.

Our controller can be easily adapted to track different classes of reference signals, and makes it possible to make the platen accomplish sophisticated maneuvers. As an illustration, we make the platen follow an ellipse in three-space not parallel to the horizontal plane, while preventing the platen from rotating. We also measure the set-point stabilization performance of our control system with steps in each axis.

Comparison to other control approaches. The linearization-based control strategy of [1] and [2] limits the range of operation of the device, the size of the step references, and the transient performance. Such shortcomings were experimentally analyzed in [11] for the case of one iron-cored PMLSM. In contrast to that, our nonlinear control approach guarantees that the closed-loop system tracks reference signals with large amplitude over the entire range of operation of the device. This desirable feature is shared by the approaches in [3], [4], [5], [6], [7], [8], [9], also relying on feedback linearization, but our control approach has two distinctive features. First, using an output regulator for the feedback linearized system, rather than a lead-lag compensator, it yields robustness against pre-specified classes of input-matched disturbances (in this work, constant and sinusoidal with given frequency). Second, antiwindup compensation avoids undesirable transient degradations in the presence of actuator saturation. In turn, this improves the set-point stabilization performance when subjecting the system to large step references (in this case, large actuator effort is required in the transient phase).

II. HARDWARE AND MODELING

Our positioning system consists of a set of four symmetrically placed iron-cored PMLSMs. A schematic exploded view of the setup is shown in Fig. 1. Each PMLSM consists of a stator and a mover. The stators, housed in a heavy, stationary frame, are longitudinally laminated and transversally slotted to accommodate a single layer of 3-phase winding. Each mover, consisting of a set of four type N35 permanent magnets, is positioned beneath a corresponding stator and affixed to the aluminum platen. The platen is positioned below the stationary frame and rests on sets of linear guides that allow it to move along two horizontal axes, one vertical axis, as well as rotate about the two horizontal axes (pitch and roll). Fig. 2 shows the schematic diagram of a stator/mover pair. As seen in Fig. 1, the sets of linear guides are layered such that the Y-axis guides rest on the Z-axis guides, which rest on the X-axis guides. The θ and ϕ rotations shown in Fig. 1 are achievable since the four vertical guides, although attached to a rigid platen, are independent and can be positioned at different heights, allowing the platen to tilt. While the vertical (Y-axis) guides are symmetric with respect to each horizontal axis, they are *not* symmetric with respect to the vertical axis through the center of mass of the platen (see Fig. 1) because they have a rectangular section. As a result, it is more difficult to rotate about the X-axis than the Z-axis; for this reason, the device can achieve a larger rotation angle about the Z-axis than about the X-axis. Currently, the rigidity of the supporting guides does not allow for rotations about the Y-axis. The linear guides are passive units: they do not provide any actuation force to the platen. They are used to facilitate the placement of sensors used to measure displacements and rotations, and to constrain the rotation about the vertical axis (yaw). They allow us to focus our attention on the feasibility of our design and the control task, leaving the issue of contactless sensing for future research. The 3DOF apparatus in [11] uses three optical encoders mounted on the linear guides to measure X-axis, Z-axis, and Y-axis displacement. For the 5DOF system there are a total of six optical encoders mounted on the guides: two sensors measuring horizontal displacements along the X-axis and Z-axis, and four sensors mounted on the four Y-axis guides that are used to measure vertical displacement and also rotations about the X-axis and Z-axis. The linear guides also allow us to insert stoppers to constrain the motion of the platen, which is useful for parameter estimation purposes. The system has an horizontal displacement range of ± 50 mm along the X-axis and Z-axis, a vertical range of 13 mm (minimum air-gap 18 mm, maximum
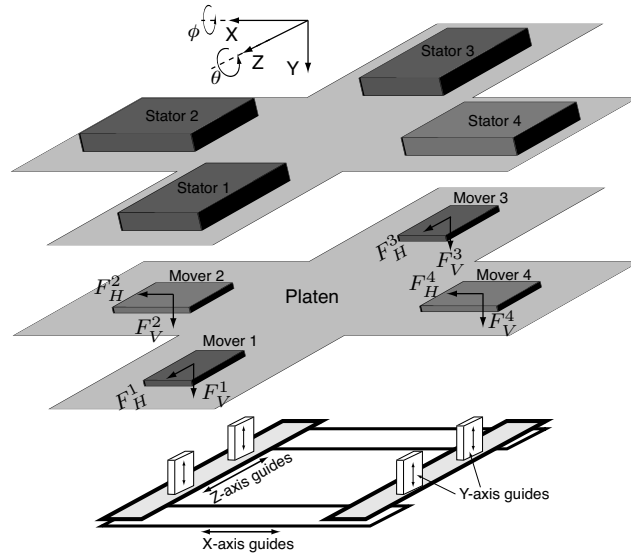
Fig. 1. Exploded schematic view of the 5DOF maglev system. The stators of four iron-cored PMLSMs, shown on top, are mounted on a stationary frame. The platen, shown in the middle, hosts the four movers and lies on three sets of orthogonally mounted linear guides, shown at the bottom. Linear guides allow for XYZ-displacements and θ, ϕ rotations, and disallow rotations about the Y-axis. Linear guides will be removed in a future-generation prototype.
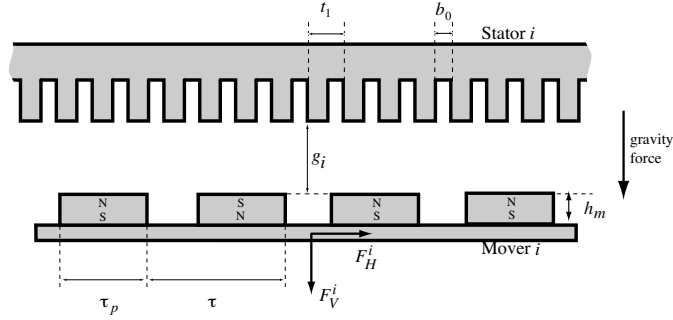

Fig. 2. Schematic side-view representation of stator/mover pair i. The slotted stator houses 3-phase windings, while the mover hosts four permanent magnets. The values and descriptions of geometric parameters t_1, b_0, h_m, τ, and τ_p, as well as other physical parameters of the device, are found in Table I. The variable g_i represents the air-gap length for Motor i. The motor produces a force on the mover whose horizontal and vertical components, F_H^i and F_V^i, have the expressions in (1) and (2).

air-gap 31 mm), and rotations about the X-axis and Z-axis of approximately ± 3 mrad and ± 14 mrad, respectively. Aside from the limitations on the rotations imposed by the rigidity of the linear guides, the maximum rotation angles are also limited at small and large air-gaps where we risk hitting the stoppers. The 5DOF apparatus has a translational resolution of 10 μm and a rotational resolution of approximately 20 μrad.

The 5DOF system uses four custom-built power supplies, developed by Quanser, each containing three linear amplifiers with voltage level of 28 V, delivering 5 A continuous and 7 A peak current. Each power supply controls the three-phase currents of a single PMLSM so that the four PMLSMs can be independently controlled. The experiment is connected to a PC by means of two Quanser Q8 data acquisition boards. The controller is implemented in Simulink and run in real-time with a sampling rate of 1kHz through the Quanser WINCON real-time environment. We refer the interested reader to [11] for more details concerning the interface between computer and experiment.

Consider the stator/mover pair of Motor i, depicted in Fig. 2. The horizontal force (F_H^i) and vertical force (F_V^i) exerted on the mover by the stator are given by

$$F_H^i(g_i, i_q) = -K_h L_h(g_i) i_q \tag{1}$$

$$F_V^i(g_i, i_q, i_d) = -K_{v1} L_{v1}(g_i) + K_{v2} L_{v2}(g_i) i_d - K_{v3} L_{v3}(g_i)(i_d^2 + i_q^2), \tag{2}$$

where

$$K_{v1} = \frac{L_A p_m \tau}{4\mu_0} \qquad L_{v1}(g_i) = \tilde{\lambda}(g)B_{pmy1}^2(g_i)$$
$$K_{v2} = \frac{3\sqrt{2}L_A p_m W k_{w1}}{p^2} \qquad L_{v2}(g_i) = \frac{\tilde{\lambda}(g)B_{pmy1}(g_i)\coth(\frac{\pi}{\tau}(h_m+g))}{K_c(g_i)} \qquad (3)$$
$$K_{v3} = \frac{18 L_A p_m W^2 k_{w1}^2 \mu_0}{\tau p^2} \qquad L_{v3}(g_i) = \frac{\tilde{\lambda}(g_i)\coth^2(\frac{\pi}{\tau}(h_m+g))}{K_c^2(g_i)},$$

and

$$K_h = \frac{12\sqrt{2}W k_{w1} p_m L_A \sigma_m \mu_0 \sinh(\frac{\pi}{\tau}h_m)\sin(\frac{\pi \tau_p}{2\tau})}{\pi p},$$

$$L_h(g_i) = \frac{\tilde{\lambda}(g_i)}{K_c(g_i)\sinh(\frac{\pi}{\tau}(h_m+g_i))},$$

$$K_c(g_i) = \frac{t_1}{t_1 - g\gamma_1(g_i)}, \qquad (4)$$

$$\gamma_1(g_i) = \frac{4}{\pi}\left[\frac{b_0}{2g_i}\arctan\left(\frac{b_0}{2g_i}\right) - \ln\sqrt{1+\left(\frac{b_0}{2g_i}\right)^2}\right],$$

$$\tilde{\lambda}(g_i) = 1 - \frac{b_0^2}{4t_1(g_i + \frac{b_0}{2} + \frac{h_m}{\mu_{rec}})}.$$

We refer the reader to [10] for the derivation of the expressions in (1)-(4). In the force expressions (1), (2), i_d and i_q represent the direct and quadrature currents applied to the three-phase winding of the stator, while g_i is the vertical air-gap, i.e., the distance between the mover and stator (see Fig. 2). Notice that the horizontal force F_H^i is independent of the horizontal displacement of the mover and thus, in particular, the model neglects the cogging force due to the slots in the stator. In [12, Section V-C] it was shown experimentally that the cogging force of our PMLSMs is negligible for air-gaps larger than 15 mm, and since the air-gap range of the 5DOF device is 18 to 33 mm, the absence of the cogging force in F_H^i is justified. The physical parameters in the above equations are given in Table I.

TABLE I
PHYSICAL PARAMETERS FOR THE 5DOF MAGLEV SYSTEM.

Parameter	Symbol	Value
Hardware dimensions	-	1.2m×1.2m×0.3m
Motor pair separation	-	400 mm
Stator slot width	b_0	12.7 mm
Stator slot pitch	t_1	19.05 mm
Turns per phase	W	900
Coil pitch	w_c	57.15 mm
Stator pole pairs	p	3 per motor
Stator slots	z_1	18 per motor
PM height	h_m	5 mm
PM length	L_A	50 mm
Number of PM's	p_m	4 per motor
Pole pitch	τ	57.15 mm
PM width	τ_p	28.58 mm
PM coercivity	H_c	875400 A/m
X-axis mover mass	M_x	10.6 kg
Z-axis mover mass	M_z	8.6 kg
Y-axis mover mass	M_y	6.9 kg
Radius to movers	r	39.7 cm
X-axis inertia	I_x	0.5268 kgm^2/rad
Z-axis inertia	I_z	0.5268 kgm^2/rad

In order to model the motion of the platen, we note that its center of mass (CM) coincides with its geometric center, and define the state vector $(x_1, \ldots, x_{10})$ as in Table II. The state x_1, the vertical displacement of the center of mass of the platen, corresponds to the average air-gap of the four PMLSMs, which we have denoted $g_1, \ldots, g_4$. Therefore, letting r denote the distance from the center of the platen to the center of the movers, we have

$$\begin{aligned} g_1 &= x_1 - r\sin x_7, \quad g_2 = x_1 + r\sin x_9, \\ g_3 &= x_1 + r\sin x_7, \quad g_4 = x_1 - r\sin x_9. \end{aligned} \qquad (5)$$

TABLE II
STATE VARIABLES AND THEIR PHYSICAL MEANING FOR THE 5DOF MAGLEV SYSTEM.

State variable	Units	Description
x_1	m	Vertical displacement of CM
x_2	m/s	Vertical velocity of CM
x_3	m	X-axis displacement of CM
x_4	m/s	X-axis velocity of CM
x_5	m	Z-axis displacement of CM
x_6	m/s	Z-axis velocity of CM
x_7	rad	Rotation angle about the X-axis (ϕ)
x_8	rad/s	Angular velocity about the X-axis
x_9	rad	Rotation angle about the Z-axis (θ)
x_{10}	rad/s	Angular velocity about the Z-axis

We combine the horizontal forces as follows. We impose that the quadrature currents for Motors 2 and 4 (lying along the X-axis) be equal, and we denote u_x the resulting quadrature current. Similarly, we impose that the quadrature currents for Motors 1 and 3 (lying along the Z-axis) be equal to a current u_z. We then let the direct currents i_d be redefined as inputs $u_{y1}, \ldots, u_{y4}$ for Motors 1 to 4, respectively. We thus have six control inputs, $u_x, u_z, u_{y1}, \ldots, u_{y4}$. The force diagram of the 5DOF system is depicted in Fig. 1.

In order to derive a model for the translational dynamics of the platen (subsystem with states $x_1, \ldots, x_6$), we must account for the fact that, due to the configuration of the linear guides, the components that move along the X, Y, and Z-axes have different masses. Accordingly, let M_x denote the mass of all components mounted on top of the X-axis linear guide (including the guide itself). Similarly, let M_y and M_z denote the masses of all components mounted on top of the Y-axis and Z-axes linear guides, respectively (including the guides themselves). Referring to Fig. 1, the X-axis guides carry the largest mass, while the Y-axis guides carry the least mass, so $M_x > M_z > M_y$. Using the expressions for the forces produced by one PMLSM in (1) and (2) and the force diagram in Fig. 1, we obtain the following model of the translational dynamics

$$
\begin{aligned}
\ddot{x}_1 = \ & G - C_{v1}L_{v1}(g_3) - C_{v1}L_{v1}(g_1) - C_{v1}L_{v1}(g_2) - \\
& C_{v1}L_{v1}(g_4) + C_{v2}L_{v2}(g_3)u_{y3} + C_{v2}L_{v2}(g_1)u_{y1} + \\
& C_{v2}L_{v2}(g_2)u_{y2} + C_{v2}L_{v2}(g_4)u_{y4} - \\
& (C_{v3}L_{v3}(g_3) + C_{v3}L_{v3}(g_1))u_z^2 - \\
& C_{v3}L_{v3}(g_3)u_{y3}^2 - C_{v3}L_{v3}(g_1)u_{y1}^2 - \\
& (C_{v3}L_{v3}(g_2) + C_{v3}L_{v3}(g_4))u_x^2 - \\
& C_{v3}L_{v3}(g_2)u_{y2}^2 - C_{v3}L_{v3}(g_4)u_{y4}^2 \\
\ddot{x}_3 = \ & -C_x\big(L_h(g_2) + L_h(g_4)\big)u_x, \\
\ddot{x}_5 = \ & -C_z\big(L_h(g_3) + L_h(g_1)\big)u_z,
\end{aligned}
\tag{6}
$$

where G denotes the acceleration due to gravity, $C_{vi} = K_{vi}/M_y$, $i = 1, 2, 3$, $C_x = K_h/M_x$, and $C_z = K_h/M_z$.

The (ϕ, θ) rotations are controlled by exerting different normal forces at opposite ends of the apparatus using Motor pairs 1/3 and 2/4, thus applying a torque about the horizontal axes. Letting I_x and I_z denote the moments of inertia about the X-axis and Z-axis (by symmetry, $I_x = I_z$), and $k_{rot} = rM_y/I_x$, and referring to Fig. 1, we obtain the model of the rotation dynamics

$$
\begin{aligned}
\ddot{x}_7 = \ & k_{rot}\big(-C_{v1}L_{v1}(g_3) + C_{v2}L_{v2}(g_3)u_{y3} - \\
& C_{v3}L_{v3}(g_3)u_{y3}^2 + C_{v1}L_{v1}(g_1) - \\
& C_{v2}L_{v2}(g_1)u_{y1} + C_{v3}L_{v3}(g_1)u_{y1}^2 - \\
& (C_{v3}L_{v3}(g_3) - C_{v3}L_{v3}(g_1))u_z^2\big) - k_{s\phi}x_7 \\
\ddot{x}_9 = \ & k_{rot}\big(-C_{v1}L_{v1}(g_2) + C_{v2}L_{v2}(g_2)u_{y2} - \\
& C_{v3}L_{v3}(g_2)u_{y2}^2 + C_{v1}L_{v1}(g_4) - \\
& C_{v2}L_{v2}(g_4)u_{y4} + C_{v3}L_{v3}(g_4)u_{y4}^2 - \\
& (C_{v3}L_{v3}(g_2) - C_{v3}L_{v3}(g_4))u_x^2\big) - k_{s\theta}x_9.
\end{aligned}
\tag{7}
$$

The output of the system is $y = \begin{bmatrix} x_1 & x_3 & x_5 & x_7 & x_9 \end{bmatrix}^\top$. The constants $k_{s\phi}$ and $k_{s\theta}$ in (7) represent torsional spring forces opposing the X-axis rotation and Z-axis rotation, respectively, modeling the effect of the Y-axis linear guides opposing rotations of the platen.

The model (6), (7) is not control-affine since the controls enter nonlinearly in $\dot{x}_2, \dot{x}_8$, and $\dot{x}_{10}$. A number of parameters in (6), (7) are either unknown or are not known with sufficient accuracy. We estimated them using an adaptation of the parameter estimation technique presented in [11]. The details are omitted due to space limitations.

III. NONLINEAR CONTROLLER DESIGN

In this section, we design a controller to track steps and sinusoidal reference signals with a given frequency ω_0. Before we can proceed with controller design, we eliminate the overactuation of the system and we show that the model can be significantly simplified by omitting terms of negligible magnitude.

Referring to the full 5DOF model in (6), (7), the horizontal dynamics (subsystem with states $x_3, \ldots, x_6$) have two control variables, u_x and u_z for two DOFs. The vertical and rotational dynamics (states $x_1, x_2, x_7, \ldots, x_{10}$) provide the remaining three DOFs with a total of four control variables: $u_{y1}, \ldots, u_{y4}$. Thus, the subsystem comprising the vertical and rotational dynamics is overactuated. To eliminate overactuation we define new control inputs (v_y, v_ϕ, v_θ) as follows,

$$
\begin{aligned}
u_{y1} = (v_y + v_\phi)/2, \quad u_{y2} = (v_y - v_\theta)/2, \\
u_{y3} = (v_y - v_\phi)/2, \quad u_{y4} = (v_y + v_\theta)/2,
\end{aligned}
\tag{8}
$$

where now, roughly speaking, v_y, v_ϕ, and v_θ are mostly responsible for the vertical translation, the X-axis rotation, and the Z-axis rotation, respectively. Applying the above input transformation to system (6), (7), we get a 5DOF model with inputs $(v_y, v_\phi, v_\theta, u_x, u_z)$ of the form

$$
\begin{aligned}
\ddot{x}_1 = {}& a_1(x_1, x_7, x_9, u_x, u_z) + a_2(x_1, x_7)v_\phi + \\
& a_3(x_1, x_7, x_9)v_y + a_4(x_1, x_7)v_\phi v_y + \\
& a_5(x_1, x_7)v_\phi^2 + a_6(x_1, x_7, x_9)v_y^2 + \\
& a_7(x_1, x_9)v_\theta + a_8(x_1, x_9)v_y v_\theta + a_9(x_1, x_9)v_\theta^2 \\
\ddot{x}_3 = {}& -C_x\big(L_h(g_2) + L_h(g_4)\big)u_x \\
\ddot{x}_5 = {}& -C_z\big(L_h(g_3) + L_h(g_1)\big)u_z \\
\ddot{x}_7 = {}& b_1(x_1, x_7, u_z) + b_2(x_1, x_7)v_\phi + b_3(x_1, x_7)v_y + \\
& b_4(x_1, x_7)v_\phi v_y + b_5(x_1, x_7)v_\phi^2 + b_6(x_1, x_7)v_y^2 \\
\ddot{x}_9 = {}& c_1(x_1, x_9, u_x) + c_2(x_1, x_9)v_\theta + c_3(x_1, x_9)v_y + \\
& c_4(x_1, x_9)v_y v_\theta + c_5(x_1, x_9)v_\theta^2 + c_6(x_1, x_9)v_y^2 \\
y = {}& \begin{bmatrix} x_1 & x_3 & x_5 & x_7 & x_9 \end{bmatrix}^\top,
\end{aligned}
\tag{9}
$$

where the functions a_i, b_j, c_k, $i = 1, \ldots 9$, $j = 1, \ldots, 6$, $k = 1, \ldots, 6$ are straightforwardly defined using the expressions for $g_1, \ldots, g_4$ in (5), the model (6), (7), and the input transformation (8). We now have a total of five inputs to control five DOFs. From now on, we will simply write $a_1, \ldots, a_9$, $b_1, \ldots, b_6$, and $c_1, \ldots, c_6$, omitting the arguments of these functions for ease of notation.

Numerical evaluation of the functions a_i, b_j, c_k reveals that certain terms in (9) are much smaller in magnitude than others over the operating range. This is illustrated for the functions a_i in Fig. 3. Fig. 3(a) depicts the result of maximizing the functions $a_2, \ldots, a_9$ with respect to the rotation angles x_7 and x_9 while setting $u_x = u_z = 0$,

$$
\begin{array}{cc}
\max_{\substack{x_7 \in [-0.003, 0.003] \\ x_9 \in [-0.014, 0.014] \\ u_x = u_z = 0}} |a_i|, & i = 2, \ldots, 9,
\end{array}
\tag{10}
$$

over an air-gap range of 20 mm to 30 mm. Fig. 3(b) zooms in on the curves with the smallest magnitudes in Fig. 3(a) to give a better perspective on their relative magnitudes. The function a_1 is not shown since its magnitude is on the order of 10^3, which is much larger than the other functions shown. Analogous considerations for the functions b_j and c_k lead to the conclusion that the vertical dynamics and rotational dynamics are dominated by certain functions: a_1, a_2, a_3, a_7 dominate the vertical dynamics, b_1, b_2, b_3 dominate the X-axis rotation dynamics, and c_1, c_2, c_3 dominate the Z-axis rotation dynamics; the functions $a_4, a_5, a_6, a_8, a_9, b_4, b_5, b_6, c_4, c_5$, and c_6 are so much smaller in magnitude that they appear to be negligible. This consideration leads us to replace the model (9) with the simplified model

$$
\begin{bmatrix} \ddot{x}_1 \\ \ddot{x}_3 \\ \ddot{x}_5 \\ \ddot{x}_7 \\ \ddot{x}_9 \end{bmatrix} = \begin{bmatrix} a_1 \\ h_x(x_1, x_9)u_x \\ h_z(x_1, x_7)u_z \\ b_1 \\ c_1 \end{bmatrix} + \begin{bmatrix} a_3 & a_2 & a_7 \\ 0 & 0 & 0 \\ 0 & 0 & 0 \\ b_3 & b_2 & 0 \\ c_3 & 0 & c_2 \end{bmatrix} \begin{bmatrix} v_y \\ v_\phi \\ v_\theta \end{bmatrix},
\tag{11}
$$

where

$$
\begin{aligned}
h_x(x_1, x_9) &= -C_x\big(L_h(g_2) + L_h(g_4)\big), \\
h_z(x_1, x_7) &= -C_z\big(L_h(g_3) + L_h(g_1)\big),
\end{aligned}
$$

with g_i defined in (5). Besides the numerical considerations above, a theoretical justification for this model simplification is
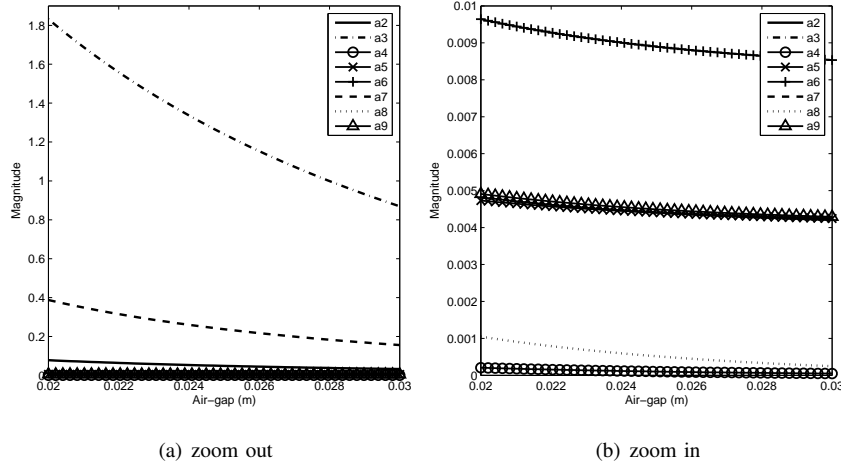
(a) zoom out   (b) zoom in

Fig. 3. Magnitude of a_i, $i = 2, \ldots, 9$ functions over a range of air-gaps and maximized with respect to rotation angles x_7 and x_9. It can be seen that the functions a_2, a_3, and a_7 dominate in magnitude a_4, a_5, a_6, a_8, and a_9.

found in [13]. Consider the nominal system (11) and the following feedback linearizing transformation,

$$\begin{bmatrix} v_y \\ v_\phi \\ v_\theta \end{bmatrix} = \begin{bmatrix} a_3 & a_2 & a_7 \\ b_3 & b_2 & 0 \\ c_3 & 0 & c_2 \end{bmatrix}^{-1} \begin{bmatrix} w_y - a_1 \\ w_\phi - b_1 \\ w_\theta - c_1 \end{bmatrix},$$

$$\begin{bmatrix} u_x \\ u_z \end{bmatrix} = \begin{bmatrix} -\dfrac{w_x}{C_x\big(L_h(g_2) + L_h(g_4)\big)} \\ -\dfrac{w_z}{C_z\big(L_h(g_3) + L_h(g_1)\big)} \end{bmatrix}, \tag{12}$$

where $w_y, \ldots, w_\theta$ are new control inputs. The state-dependent matrix in (12) can be numerically shown to be invertible in the range of operation of the system and the denominators in the expressions for u_x and u_z in (12) are non-zero within the operating range. The closed-loop system is comprised of five decoupled double-integrators; the input is $(w_y, w_x, w_z, w_\phi, w_\theta)$ and the output is y,

$$\ddot{x}_1 = w_y \quad \ddot{x}_3 = w_x \quad \ddot{x}_5 = w_z \quad \ddot{x}_7 = w_\phi \quad \ddot{x}_9 = w_\theta$$
$$y = [x_1 \ \ x_3 \ \ x_5 \ \ x_7 \ \ x_9]^\top. \tag{13}$$

We now apply the output regulation theory of [14], [15], [16] to (13). The control objective is to stabilize set-point references, track sinusoidal references with fixed frequency ω_0, or a combination of the two. Since (13) comprises five decoupled linear systems, each with two poles at the origin, it would be sufficient, in principle, to use internal models with poles at $\pm i\omega_0$. In order to provide robustness against constant input disturbances, we also include a pole at the origin. The output regulator incorporates five copies of the following internal model with poles at $\pm i\omega_0$ and 0,

$$\dot{\xi}_s = \Phi\xi_s + Ne_s, \quad w_s = \Gamma\xi_s, \quad s \in \{'y', 'x', 'z', '\phi', '\theta'\}, \tag{14}$$

where

$$\Phi = \begin{bmatrix} 0 & 1 & 0 \\ 0 & 0 & 1 \\ 0 & -\omega_0^2 & 0 \end{bmatrix}, \quad N = \begin{bmatrix} 0 \\ 0 \\ 1 \end{bmatrix}, \quad \Gamma = [\ 1 \ \ 0 \ \ 0\ ], \tag{15}$$

and $e_y = x_1 - x_1^{\text{ref}}$, $e_x = x_3 - x_3^{\text{ref}}$, $e_z = x_5 - x_5^{\text{ref}}$, $e_\phi = x_7 - x_7^{\text{ref}}$, $e_\theta = x_9 - x_9^{\text{ref}}$ denote the tracking errors. The regulator design is completed by letting

$$w_s = K_s[e_s \ \ \dot{e}_s \ \ \xi_s]^\top + \Gamma\xi_s, \quad s \in \{'y', 'x', 'z', '\phi', '\theta'\}. \tag{16}$$

The state feedback controller gains $K_y, K_x, K_z, K_\phi, K_\theta$ are chosen to stabilize the closed-loop system when the reference signals $x_1^{\text{ref}}, \ldots, x_5^{\text{ref}}$ are set to zero. The derivative signals $\dot{e}_y, \ldots, \dot{e}_\theta$ are estimated from the measured $e_y, \ldots, e_\theta$ by means of linear filters, as in [11]. We also include saturation and antiwindup compensators for the horizontal X-axis and Z-axis regulators since large step references for the horizontal translations result in large translational accelerations. These large accelerations demand a larger sustained current from the power supplies, which are only capable of providing 5 A of sustained current and 7 A peak current. Thus, when large horizontal steps are commanded, the amplifiers' supply of direct current, which generates the PMLSM normal forces, drops significantly. Letting $\text{sat}_7(u)$ denote the saturation function with saturation limits at ± 7, the

antiwindup modifications for the X and Z-axes internal models are defined as

$$\dot{\xi}_s = \Phi\xi_s + Ne_s + E_s\big(\text{sat}_7(u_s) - u_s\big), \ w_s = \Gamma\xi_s, \ s \in \{'x', 'z'\}, \tag{17}$$

where E_x and E_z are antiwindup compensator gains that are manually tuned to give the desired antiwindup performance (stability and minimal overshoot) for aggressive internal model regulator design (fast transients, minimal steady-state error). The final controller is given by (8), (12), (14), (16), and (17).

IV. Experimental Results

As mentioned in Section II, the range of rotation about the X-axis is smaller than that about the Z-axis due to the asymmetry of the vertical guides. Moreover, the torsional spring constant associated with X-axis rotation is large, which means larger currents are required to perform rotations. Therefore, we will implement a regulator for the X-axis rotation to regulate that angle to zero and only show experimental results for set-point stabilization and sinusoidal tracking for the Z-axis rotation, which has a much larger range of operation and smaller torsional spring constant. We stress that experimental results for the Z-axis rotation give similar results to those associated with the X-axis rotation, the main differences being a degradation in performance and reduced range of X-axis rotations. We also stress that once the linear guides are removed from the apparatus, the adverse effect of linear guides on rotations will disappear and there should be no difference between X-axis and Z-axis rotations.

A. Set-Point Stabilization

Recall that the controller given by (12), (14), (16), and (17) simultaneously achieves set-point stabilization and sinusoidal tracking for the nominal system (11). We begin by performing various set-point stabilization experiments. The values chosen for $K_y, K_x, K_z, K_\phi, K_\theta$ were generated using LQR design with manual tuning of the weight matrices. We choose performance specifications for the 3DOF translations (XYZ) to match the specifications given for the 3DOF system in [11], so that we can compare the 5DOF system performance with the 3DOF system in [11]. The performance goals of the set-point tracking controller are as follows:

(1) The tracking controller should be able to stabilize set-points within the operating range of [20 mm, 30 mm] for the Y-axis translation, [-30 mm, 30 mm] for the X and Z-axis translations, and [-10 mrad, 10 mrad] for the Z-axis rotation. The controller must stabilize steps as large as 5 mm for the Y-axis, 30 mm for the X and Z-axis, and 10 mrad for the Z-axis rotation.

(2) The overshoot (%OS) should ideally be less than 30% for steps within the limits mentioned above.

(3) For translation set-points within the specified limits, let t_s denote the time it takes for the tracking error to go and stay below 0.1 mm, and t_{enc} denote the time it takes for the tracking error to reach encoder resolution of 10 μm. We want $t_s < 3$ sec and $t_{\text{enc}} < 10$ sec.

(4) For Z-axis rotational set-points within the specified limits, let t_s denote the time it takes for the tracking error to go and stay below 0.1 mrad and t_{enc} the time it takes to reach encoder resolution of 20 μrad. We want $t_s < 3$ sec and $t_{\text{enc}} < 10$ sec.

We begin by performing set-point stabilization for the 3DOF translational subsystem (states $x_1, \ldots, x_6$). The rotation controls are disabled ($v_\phi = v_\theta = 0$) to ensure that all four motors produce equal normal forces to lift the platen evenly. To determine the regulator gains, we tune LQR weight matrices and the resulting closed-loop poles of the $(e_y, \dot{e}_y, \xi_y)$ subsystem are $[-173.2, -2.61 \pm i\,5.48, -2.16 \pm i\,1.77]$ and the closed loop poles of the $(e_x, \dot{e}_x, \xi_x)$ and $(e_z, \dot{e}_z, \xi_z)$ subsystems are $[-38.73, -3.2 \pm i\,5.89, -2.69 \pm i\,2.23]$. The manually tuned antiwindup compensator gains are $E_x = E_z = 7 \times 10^{-5}[1 \ 1 \ 1]^\top$.

The air-gap x_1 and absolute air-gap error $|x_1 - x_1^{\text{ref}}|$ are shown in Fig. 4. The transient performance is well within specifications, even when the system is subjected to a large step reference of 7 mm. The results for horizontal displacements x_3 and x_5 are entirely analogous and are omitted due to space limitations. The controller gains can be tuned to reduce the settling time at the expense of increased overshoot. To reduce the overshoot for step references we can choose to accept a longer settling time or reduce the step size. This trade-off between overshoot and settling time was also observed in [11]. The performance of the translational subsystem matches the results obtained in [11] for the 3DOF translational system and meets all performance specifications.

Next, we control the rotation about the Z-axis. We restrict the horizontal motion of the platen in hardware so that the platen can only move along the vertical Y-axis and rotate. Since we cannot fix the center of mass of the platen without also restricting rotations, we use the Y-axis regulator to maintain a constant air-gap of 25 mm. Throughout these tests there is negligible deviation from the desired air-gap. After tuning the rotation regulator gains using LQR, the closed-loop poles of the $(e_\theta, \dot{e}_\theta, \xi_\theta)$ subsystem are $[-200, -2.81 \pm i\,5.58, -2.19 \pm i\,1.82]$. A series of step commands are issued to the Z-axis rotation (angle θ), and the results are shown in Fig. 5. Although we are able to achieve steady-state errors of under 0.1 mrad in under 3 seconds (t_s) for 5 mrad steps, we are not able to achieve this same performance for 10 mrad steps. The unmodeled effects of the vertical guides on the rotational dynamics and the large step sizes are the main reasons why we fail to meet this particular performance specification. However, the steady-state error for 10 mrad steps does reach 0.1 mrad in under 5 seconds so the performance is considered acceptable. For all steps up to 10 mrad the steady-state error reaches encoder resolution in under 10 seconds (t_{enc}),
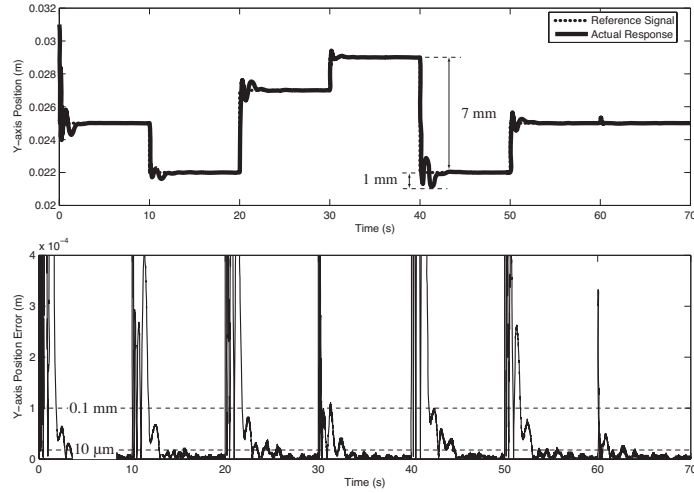
Fig. 4. Vertical air-gap response and error for 3DOF set-point stabilization. The system meets all performance specifications. When subjected to a large step reference of 7 mm, the overshoot is 1 mm, or 14.3%, and the absolute tracking error settles below 0.1 mm in less than 3 sec., and to encoder resolution of 10 μm in about 5 sec.
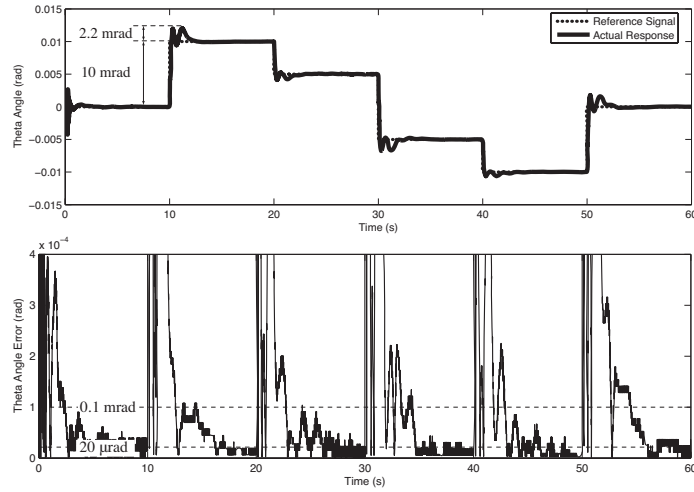

Fig. 5. Z-axis rotation response and error for 1DOF set-point stabilization. In response to a 10 mrad step, the system has an maximum overshoot of 2.2 mrad, or 22%, and the absolute tracking error settles below 0.1 mrad in less than 5 sec, and to encoder resolution of 20 μrad in less than 10 sec, but it occasionally fluctuates about 20 μrad. This fluctuation is likely due to the adverse effect of the Y-axis guides on rotational dynamics.

but occasionally fluctuates about the rotational encoder resolution. This is likely due to the unmodeled effects of the vertical guides on the rotational dynamics. Removal of the supporting guides will eliminate the undesired effects of the vertical guides and likely improve the performance of the rotational dynamics. Higher resolution encoders should also significantly improve the steady-state error. Similar set-point stabilization experiments for the X-axis rotation (results omitted) exhibit a degraded performance and a smaller range of operation compared to the Z-axis rotation, which is due to the increased effects of the vertical guides opposing rotations (see discussion in Section II). As with translational set-point stabilization, there is a trade-off between overshoot and settling time; by tuning our controller gains we can choose to minimize one or the other.

The results of all set-point stabilization experiments are summarized in Table III.

B. Sinusoidal Tracking

We apply sinusoidal reference signals with a frequency $\omega_0 = 1.5\pi$ rad/s; this frequency was chosen to match the frequency used in [11] so that the results of the 5DOF system can be compared to the 3DOF results in [11]. Using the same controller

TABLE III
SET-POINT STABILIZATION RESULTS.

DOF	%OS	t_s	t_{enc}
Y-ax. translation	<30%	<3 sec	<10 sec
X-ax. translation	<30%	<3 sec	<10 sec
Z-ax. translation	<30%	<3 sec	<10 sec
Z-ax. rot. (5 mrad steps)	<30%	<3 sec	<10 sec
Z-ax. rot. (10 mrad steps)	<30%	3 to 5 sec	<10 sec

gains developed for set-point stabilization, the following reference commands are used to actuate the Y-X/Z-axis translations,

$$x_1^{\text{ref}}(t) = 0.005 \sin(1.5\pi t - \pi/2) + 0.025,$$
$$x_3^{\text{ref}}(t) = 0.03 \sin(1.5\pi t - \pi/2),$$
$$x_5^{\text{ref}}(t) = 0.03 \sin(1.5\pi t)$$
$$x_7^{\text{ref}}(t) = 0,$$
$$x_9^{\text{ref}}(t) = 0.$$

The curve $t \mapsto (x_1^{\text{ref}}(t), x_3^{\text{ref}}(t), x_5^{\text{ref}}(t))$ is an ellipse in the XYZ space. Fig. 6 shows the system response in XYZ coordinates and the path generated by the reference trajectory.
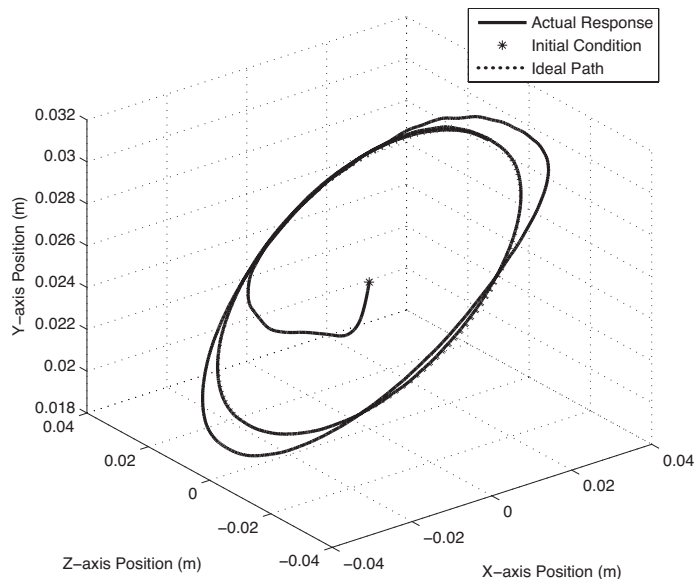

Fig. 6. 3DOF sinusoidal tracking results shown in 3-D XYZ coordinates.

It is clear from the sinusoidal tracking results that the controller is able to track the given sinusoidal references. To gauge how well the controller performs we can measure the average steady-state position errors ($|x_1^{\text{ref}}(t) - x_1(t)|$, $|x_3^{\text{ref}}(t) - x_3(t)|$, and $|x_5^{\text{ref}}(t) - x_5(t)|$) over a 60 second trial for each axis. The average position errors for the Y, X, and Z-axis are $x_1^{\text{err}} = 33.04\mu$m, $x_3^{\text{err}} = 78.33\mu$m, and $x_5^{\text{err}} = 68.25\mu$m. These results show a reduction in the steady-state tracking errors compared to the 3DOF sinusoidal tracking results in [11].

Next, we test the tracking performance when the three translations and the Z-axis rotation are simultaneously subjected to sinusoidal references,

$$x_1^{\text{ref}}(t) = 0.005 \sin(1.5\pi t - \pi/2) + 0.025,$$
$$x_3^{\text{ref}}(t) = 0.03 \sin(1.5\pi t - \pi/2),$$
$$x_5^{\text{ref}}(t) = 0.03 \sin(1.5\pi t),$$
$$x_7^{\text{ref}}(t) = 0,$$
$$x_9^{\text{ref}}(t) = 0.01 \sin(1.5\pi t).$$

Fig. 7 shows the response of the air-gap displacement x_1, and Fig. 8 shows the response of the Z-axis rotation angle. The responses for the horizontal displacements x_3 and x_5 are entirely analogous to the x_1 response, and are omitted due to space limitations. The average errors measured over 60 seconds are $x_1^{\text{err}} = 47.03\mu$m, $x_3^{\text{err}} = 77.98\mu$m, $x_5^{\text{err}} = 76.85\mu$m, and

$x_9^{\text{err}} = 123.9\mu\text{rad}.$
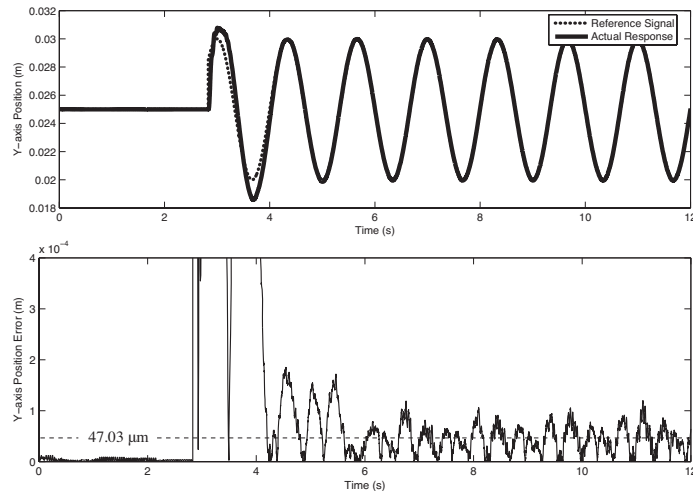

Fig. 7. Y-axis response and error for 4DOF sinusoidal tracking. The average absolute tracking error is 47.03 μm.
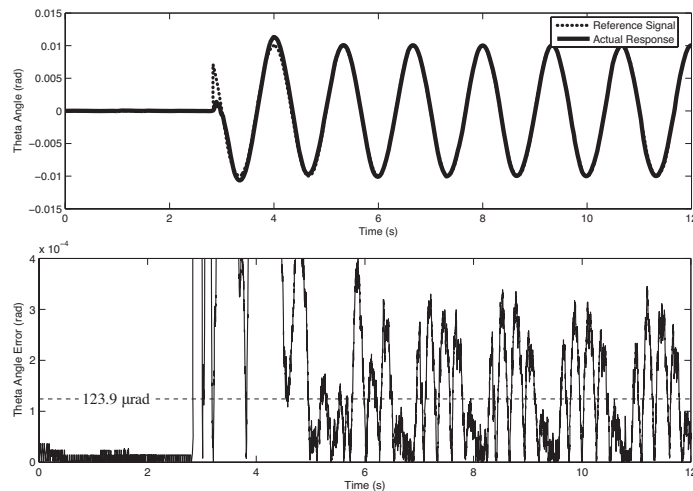

Fig. 8. Z-axis rotation response and error for 4DOF sinusoidal tracking. The average absolute tracking error is 123.9 μrad.

With the system tracking sinusoids in 4DOF, the average tracking errors for the horizontal translations and the Z-axis rotation are within 5% of the previously measured values. The vertical tracking error, however, worsens significantly (although it is still by far the lowest average error). This can be attributed to the addition of a rotation, which is highly coupled with the vertical translation. Again, removal of the vertical guides may play a significant role in reducing the tracking error. Finally, the stability of the closed-loop system, while tracking sinusoidal references covering the operating range, further validates the model simplification (11).

V. Conclusions

In this paper, the problem of controlling translations and rotations (pitch and roll) of a magnetically levitated positioning system using iron-cored PMLSMs has been addressed. The internal model regulator controller design successfully stabilizes set-point references and tracks sinusoidal references of a given frequency for XYZ translations and rotations about the X-axis and Z-axis. The results indicate that it is possible to remove the linear guide system supporting the platen and achieve fully contactless levitation with 5 degrees-of-freedom. It is noted that we have not addressed the issue of controlling the yaw of the platen. Controlling the yaw (or at least constraining this rotation) is necessary in order to ensure the current apparatus can operate without supporting linear guides. Control of the yaw rotation as well as the implementation of contactless sensing equipment for output measurement will be the subject of future research.

ACKNOWLEDGMENT

REFERENCES

[1] W. Kim and D. Trumper, "High-precision levitation stage for photolithography," *Precision Engineering*, vol. 22, pp. 66–77, 1998.

[2] W. Kim, D. L. Trumper, and J. H. Lang, "Modeling and vector control of planar magnetic levitator," *IEEE Transactions on Industry Applications*, vol. 34, no. 6, pp. 1254–1262, November/December 1998.

[3] S. Verma, W. jong Kim, and H. Shakir, "Multi-axis maglev nanopositioner for precision manufacturing and manipulation applications," *IEEE Transactions on Industry Applications*, vol. 41, no. 5, pp. 1159–1167, 2005.

[4] S. Verma, W. jong Kim, and J. Gu, "Six-axis nanopositioning device with precision magnetic levitation technology," *IEEE/ASME Transactions on Mechatronics*, vol. 9, no. 2, pp. 384–391, 2004.

[5] J. Gu, W. jong Kim, and S. Verma, "Nanoscale motion control with a compact minimum-actuator magnetic levitator," *Journal of Dynamic Systems, Measurement, and Control*, vol. 127, pp. 433–442, 2005.

[6] X. Shan, S.-K. Kuo, J. Zhang, and C.-H. Menq, "Ultra precision motion control of a multiple degree of freedom magnetic suspension stage," *IEEE/ASME Transactions on Mechatronics*, vol. 7, no. 1, pp. 67–78, March 2002.

[7] S.-K. Kuo, X. Shan, and C.-H. Menq, "Large travel ultra precision x-y-θ motion control of a magnetic suspension stage," *IEEE/ASME Transactions on Mechatronics*, vol. 8, no. 3, pp. 334–341, 2003.

[8] S.-K. Kuo and C.-H. Menq, "Modeling and control of a six-axis precision motion control stage," *IEEE/ASME Transactions on Mechatronics*, vol. 10, no. 1, pp. 50–59, 2005.

[9] Z. Zhang and C.-H. Menq, "Six-axis magnetic levitation and motion control," *IEEE Transactions on Robotics*, vol. 23, no. 2, pp. 196–205, 2007.

[10] M. Maggiore and R. Becerril, "Modeling and control design for a magnetic levitation system," *International Journal of Control*, vol. 77, no. 10, pp. 964–977, 2004.

[11] R. B. Owen and M. Maggiore, "A high-precision, magnetically levitated positioning stage: Toward contactless actuation for industrial manufacturing," *Control Systems Magazine*, vol. 26, no. 3, pp. 82–95, 2006.

[12] ——, "Implementation and model verification of a magnetic levitation system," in *Proc. American Control Conference*, Portland, OR, 2005, pp. 1142–1147.

[13] C. Fulford, "Control of a high-precision positioning system using magnetic levitaion," Master's thesis, University of Toronto, 2007.

[14] E. J. Davison, "The robust control of a servomechanism problem for linear time-invariant multivariable systems," *IEEE Transactions on Automatic Control*, vol. 21, pp. 25–34, 1976.

[15] B. A. Francis, "The linear multivariable regulator problem," *SIAM Journal on Control and Optimization*, vol. 14, pp. 486–505, 1977.

[16] B. A. Francis and W. M. Wonham, "The internal model principle of control theory," *Automatica*, vol. 12, pp. 457–465, 1976.